



Accuracy Assessment of Establishing 3D Real Scale Model in Close-Range Photogrammetry with Digital Camera

Ali H. Hadi *, Abbas Z. Khalaf 

Civil Engineering Dept., University of Technology-Iraq, Alsina'a street, 10066 Baghdad, Iraq.

*Corresponding author Email: bce.19.53@grad.uotechnology.edu.iq

HIGHLIGHTS

- Determination of Three-dimensional (3D) real scale model coordinates.
- Determination of camera interior orientation parameters (IOPs).
- Determination of camera exterior orientation parameters (EOPs).
- The bundle block adjustment method (BBA) is used in photogrammetric processing based on the collinearity equation.
- Assessment of results through statistical analysis showed a reliable accuracy where the overall accuracy of work is 5 mm.

ABSTRACT

Three-dimensional (3D) real-scale models delivered from digital photogrammetric techniques have rapidly increased to meet the requirements of many applications in different fields of daily life. This paper deals with establishing a 3D real-scale model from a block of images (18 images) captured using a Canon EOS 500D digital camera to cover a test field area consisting of 90 artificial target points, 25 of which are ground control points (GCPs). At the same time, the remains are checkpoints (CPs). The analytical photogrammetric processes, including the calculation of interior orientation parameters (IOPs) of the camera during the camera calibration process and exterior orientation parameters (EOPs) of the camera in each capture. The model's object space (ground) coordinates are calculated simultaneously based on the collinearity equation using the bundle block adjustment method (BBA). Assessment and validation of the accuracy of the results is an important task in this study that was implemented to determine and analyze the errors of 3D coordinates through linear regression analysis (LRA). Root mean square error (RMSE) is the statistical parameter used in the statistical analysis of results. The standard error is another statistical parameter used to evaluate the accuracy of camera locations and rotation angles (EOPs). The total RMSE (RMSE) xyz of GCPs is ± 2.530 mm, while the total RMSE (RMSE_{xyz}) of CPs is ± 2.740 mm. The overall accuracy of the work is 5.000 mm.

ARTICLE INFO

Handling editor: Mohammed A. Al-Neami

Keywords:

close-range photogrammetry; digital photogrammetry; 3D real scale model; bundle adjustment; collinearity equation.

1. Introduction

Photogrammetry is a branch of technology, art, and science in which accurate and precise results are attained by recording, measuring, and interpreting emitted electromagnetic energy and topographic images created by physical objects and reflected beams from their surroundings [1]. As the definition of photogrammetry indicates, the major aspect of this science is that measurements are implemented on the object's projection rather than directly done on it [2]. The main goal of Photogrammetry is to create a three-dimensional (3D) model from aerial or terrestrial images [3]. The photogrammetry technique involves registering and analyzing various images taken from various viewpoints to create a 3D reconstruction of measured objects' shape, size, and mutual location. This may be accomplished by either rotating the object within the field of view or moving the camera around it. It is feasible to recreate the surface of the inspected object by detecting the displacement of certain features between photos and establishing

their absolute position in 3D space [4]. Photogrammetry is the most accurate and practical technology for representing the real-world environment in 3D modeling [3].

Generally, aerial photogrammetry and terrestrial photogrammetry are the two types of photogrammetry. In aerial photogrammetry, images are obtained by overhead photographs from an airplane producing topographic maps and land use details. In contrast, terrestrial photogrammetry uses photographs taken near or on the earth's surface to offer detailed dimensions information about an object. Terrestrial photogrammetry is described as close-range photogrammetry when the object size and camera-to-object distance are less than 100 meters [1]. Photogrammetry has several advantages over more traditional land

surveying approaches. Firstly, objects or things inaccessible or too risky to get on foot can be mapped. Secondly, photogrammetry provides a flexible framework in which all data required for mapping may be obtained instantly, indefinitely, and at a low cost with a single image session. The mapping technique can then be used at any moment after that. Compared to traditional surveying or geodetic approaches, Photogrammetry has a third advantage: cost-effectiveness. Finally, photogrammetry generates a variety of digital deliverables, including maps, digital elevation models (DEMs), and orthophotos [5].

Digital close-range photogrammetry (DCRP) is useful and utilized in a variety of applications, including mapping [6], 3D modeling [7, 8], and generating and establishing digital products such as orthophotos [9], DEMs [10], DSMs [11], DTMs [12]. Also, it is used in topography and landslide measurements [1], monitoring slope displacement [5], buildings and structures deformation monitoring [13], and traffic accident management [14]. Moreover, digital close-range photogrammetry is widely used in industry [15, 16, 17, 18, 19], archaeology [20], architectural and cultural heritage documentation [21, 22], agriculture [23], mineralogy [24], and clinical and medical applications [25].

The 3D coordinate determination in photogrammetry is based on 3 point co-linearity equation which essentially asserts that the object point, projective camera center, and image point all lie on a straight line based on central projection [3, 26].

Different methods are applied for building and reconstructing 3D models using photogrammetry techniques, particularly close-range photogrammetry in various domains, such as building 3D models using a digital camera presented by Aysar Jameel et al. 2013 [27] to establish 3D by using an object of face-shaped clay with (5563) 3D points and 1 mm sampling rate the maximum residual equals to 0.70 pixels. Also, Abbas Z. Khalaf and Al-Saedi Ali [28] presented a study to assess the distortion that occurs during projects execution in comparison with charts and designs and detect the problem by using digital close-range photogrammetry with high precision to decide whether to keep or stop working to achieve accuracy ranges between 0.18 – 1.77 mm. A. A. Belmonte et al. [10] generated an accurate DEM with RMSE as low as 0.039 meters. Python Photogrammetry Toolbox (PPT) was used in this study to generate 3D point cloud data from images of an open pit excavation. The PPT was extended to add an algorithm converting the generated point cloud data into a usable DEM. A. Z. Khalaf et al. [20] presented research to evaluate the feasibility of applying 3D modeling of the CRP in documenting archaeological monuments. The total error in the scale bar was 0.005253 meters, whereas the total error of points was 0.010957 meters, and the accuracy for all points was 0.005 meters. Tariq N. Ataiwe et al. [29] used a smartphone camera for 3D modeling. The error in three directions was $X_{err.} = 0.292$ m, $Y_{err.} = 0.38577$ m, $Z_{err.} = 0.2889$ m while the total error was 0.563 m. Zaide Duran and Muhammed Enes Atik 2021 [3] generated a 3D model using different methods and programs, and the accuracy for 3D modeling was at different levels. Agisoft Lens gives the lowest error value. Root means square error (RMSE)_{xyz} was 0.077 mm.

The emphasis of this study is to assess and validate the accuracy of the establishment of a 3D real scale model by implementing the photogrammetric processes to determine the interior orientation parameters (IOPs), exterior orientation parameters (EOPs), and 3D object space coordinates of model points delivered from a block of 18 - 2D images using bundle block adjustment method (BBA) based on collinearity equation. Eventually, the results are analyzed statistically and assessed. Also, this study utilized photogrammetric processing to produce the real scale model, digital elevation model (DEM), and orthoimage for the test field area.

2. Materials and Methods

2.1 Test Field Area

The test field area consists of a grid of ninety artificial targets well distributed in two adjacent walls. These targets are circle targets divided into four parts with a specific center. The targets are in seven rows and thirteen columns, as shown in Figure 1. All targets' 3D ground coordinates (X, Y, Z) are measured using a total station instrument (TOPCON GPT 3105N).



Figure 1: Test Field Area

2.2 Digital Close-Range Photogrammetry

Digital close-range Photogrammetry (DCRP) is a measuring method to obtain 3D spatial information about an image-captured object. Rather than measuring the object directly, this method generates measurements from digital photographs [5]. Because it is based on the computer processing of photogrammetric images, digital photogrammetry is a highly practical domain [30]. Close-range photogrammetry allows for the extraction of three-dimensional coordinates of an object from two-dimensional digital photographs in a rapid, highly accurate, highly efficient, good stable, contactless, reliable, flexible, and large measurement range, and the economical way [1, 15]. The central perspective projection is the fundamental concept for modeling in digital close-range photogrammetry. The primary coordinate system is positioned arbitrarily in object space, whereas the secondary system originates at the perspective center X_o of the camera. Its z-axis corresponds with the principal axis and is directed away from the imagined plane Figure 2. The scale factor is set to unity. In the primary system, we have the coordinates of the perspective center, X_o , (X_o, Y_o, Z_o) , and an object point in space (X_A, Y_A, Z_A) . The projection of X_A , through X_o , in the image plane, represented in the secondary system, gives the coordinates of point X_a : $(X_a, Y_a, -c)$, where c is the principal distance between X_o and principal point, P' [1, 31]. The computer determines the position of the points using image recognition technology. Then the coordinates of the points and camera position information may be retrieved using collinearity equation and space intersection mathematical models. The data processing procedure in the working process of close-range photogrammetry is depicted in Figure 3.

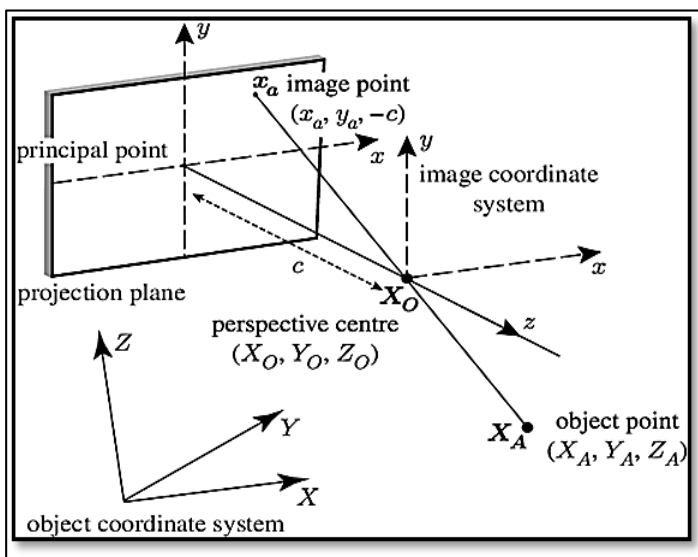


Figure 2: The Central Perspective Projection [31]

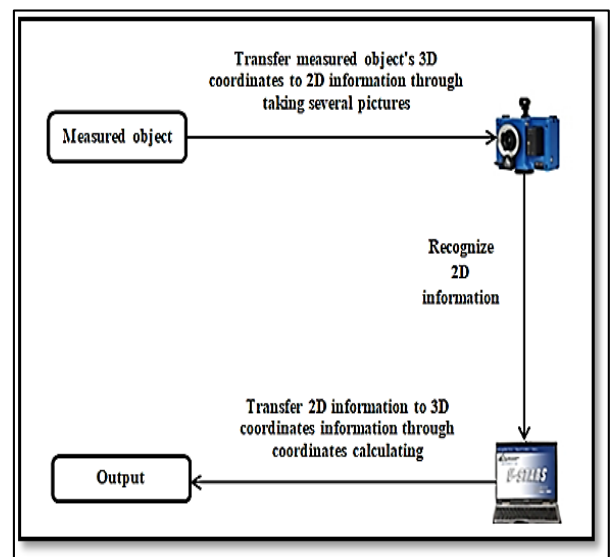


Figure 3: Data processing in close-range photogrammetry [15]

2.3 Bundle Adjustment

The workhorse of modern photogrammetry, the bundle adjustment, is a mathematical model that allows the simultaneous determination of camera exterior orientation parameters (camera position and camera orientation) (EOPs), object point coordinates (object space coordinates), and camera interior orientation parameters (camera calibration parameters) (IOPs) see Figure 4 below. Any of these can be either presented as fixed if there is prior knowledge of their numerical values or evaluated as part of the least-squares solution [32, 33, 34].

The collinearity equation is used in photogrammetric bundle adjustment (BA) to describe the world-to-camera projection [35]. The term, bundle adjustment, derives from the 'bundles' of light rays leaving each 3D feature and converging on each camera center, which are ideally 'adjusted' with regard to both feature and camera locations; this is the original information utilized in photogrammetry. Alternatively (in contrast to independent model methods, which integrate partial reconstructions without updating their internal structure), all structure and camera parameters are adjusted jointly 'in one bundle' (simultaneously) [33, 36]. The simultaneous approach combines block triangulation and adjustment into a single phase. The desired parameters are adjusted as an outcome of one simultaneous least-squares adjustment of the m photos (strip or block). The operation is often called the Bundle Block Adjustment (BBA) or simply Bundle adjustment (BA) [37]. The bundle adjustment approach is preferred over alternative methods because of its *flexibility*; it covers a broad range of 3D feature and camera kinds, scene types, information sources, and error models gracefully *accuracy*; bundle adjustment produces accurate, precise, and interpretable results, and *efficiency*; even on very big problems, mature bundle algorithms are relatively efficient [33]. The perspective attribute of the metric photos is the mathematical model of the bundle block adjustment. As the formula, the collinearity equation is utilized [36]. Bundle adjustment uses the well-known collinearity equations, or coplanarity condition, to create two equations for each measured imaging point and gives a unique solution for the system of observation equations using the least-squares approach. The collinearity equations can be written as [37]:

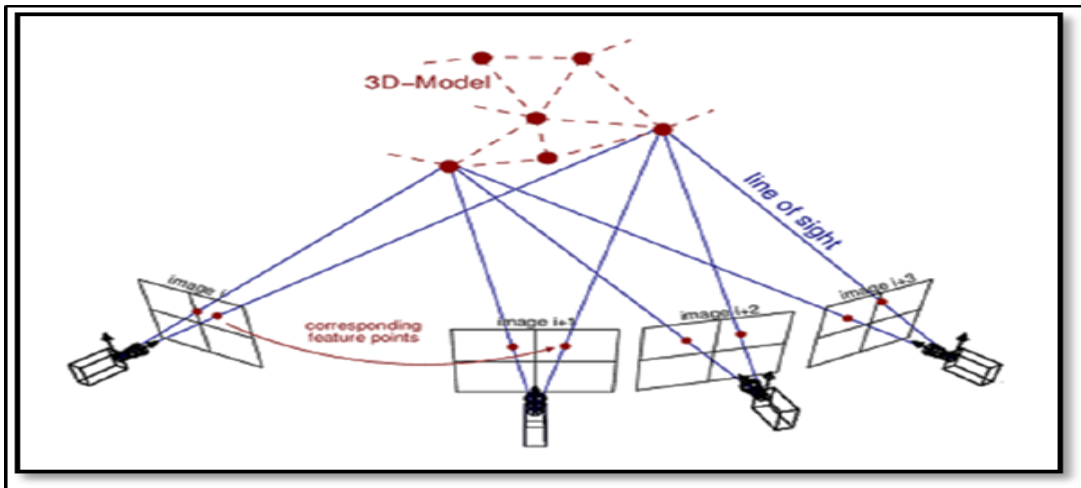


Figure 4: Typical camera configuration of bundle adjustment in close-range photogrammetry[34]

$$\begin{aligned}
 & \mathcal{X}_p + F(k) \cdot \mathcal{X}_p + F(p) \cdot \{p_1(r_p^2 + 2\mathcal{X}_p^2) + p_2(2\mathcal{X}_p \cdot \mathcal{Y}_p)\} \\
 & = -f \left[\frac{m_{11}(X - X_L) + m_{12}(Y - Y_L) + m_{13}(Z - Z_L)}{m_{31}(X - X_L) + m_{32}(Y - Y_L) + m_{33}(Z - Z_L)} \right]
 \end{aligned} \tag{1}$$

$$\begin{aligned}
 & \mathcal{Y}_p + F(k) \cdot \mathcal{Y}_p + F(p) \cdot \{p_1(r_p^2 + 2\mathcal{Y}_p^2) + p_2(2\mathcal{X}_p \cdot \mathcal{Y}_p)\} \\
 & = -f \left[\frac{m_{21}(X - X_L) + m_{22}(Y - Y_L) + m_{23}(Z - Z_L)}{m_{31}(X - X_L) + m_{32}(Y - Y_L) + m_{33}(Z - Z_L)} \right]
 \end{aligned} \tag{2}$$

$$\mathcal{X}_p = \mathcal{X}_p^- - \mathcal{X}_o \tag{3}$$

$$\mathcal{Y}_p = \mathcal{Y}_p^- - \mathcal{Y}_o \tag{4}$$

where: \mathcal{X}_p^- , \mathcal{Y}_p^- are the measured photo coordinates of image point p, \mathcal{X}_o , \mathcal{Y}_o are the photo coordinates of the principal point, f is the camera focal length, X_L , Y_L , Z_L are the object space coordinates of the camera station, X , Y , Z are the object space coordinates of the object point P, m_{11} , ..., m_{33} are the elements of photo orientation matrix.

$$r_p^2 = \mathcal{X}_p^2 + \mathcal{Y}_p^2 \tag{5}$$

$$F(k) = k_o + kr_1^2 + kr_2^4 + kr_3^6 + \dots \tag{6}$$

= function of symmetrical radial lens distortion; K_o , K_1 , K_2 , and K_3 are correction coefficients for radial lens distortion.

$$F(p) = 1 + p_3r_p^2 + p_4r_p^4 + \dots \tag{7}$$

= function of symmetrical decentering lens distortion; P_1 and P_2 are correction coefficients for decentering lens distortion.

The collinearity equation has three sets of parameters. First: camera interior orientation parameters (IOPs), second: Camera exterior orientation parameters (EOPs), and three: object space coordinates of points. Based on the parameters mentioned earlier, two methods of block adjustment as follows, different in their principles, will arise:

2.3.1 Case 1

When camera interior orientation parameters are known, the block adjustment is called simultaneous or bundle block adjustment.

2.3.2 Case 2

When camera interior orientation parameters are unknown, the block adjustment is called self-calibration block adjustment [37].

2.4 Camera Calibration

Camera calibration is a traditional problem in the field of photogrammetry. Camera calibration can be considered the inverse of the photogrammetric process. The orientation parameters are known, and the coordinates of the object points are searched (unknown) in the photogrammetric process. In contrast, in camera calibration, the coordinates of the object points are known, and the elements of the internal orientation are searched (unknown) [3]. Camera calibration is implemented to determine the camera's interior orientation parameters (IOPs). Interior orientation parameters are calibrated focal length c , coordinates of principal point coordinates (x_0, y_0) , and distortion parameters (tangential distortion parameters noted as P [P_1, P_2] and radial distortion parameters noted as K [K_1, K_2, K_3]) [3, 32] were determined with the bundle block adjustment [38]. Calibration of the camera is required for photogrammetric determination of object points (points coordinates). High accuracy cannot be attained without calibration, especially for lenses with short focal lengths, such as wide-angle lenses [32]. The quality and precision of all subsequent photogrammetric operations, such as calculating the spatial coordinates of individual points or 3D modeling, are greatly influenced by the accuracy of photo orientation and camera calibration [39]. Calibration is generally performed in three ways: pre- (laboratory) calibration, on-the-job calibration, and self-calibration [40]. Pre (laboratory) calibration method is designed for metric cameras and rarely used in close-range photogrammetry, which is cheaper and easier to apply. In this method, a lab test field of a very well-identified control system is used to calibrate the camera. On the-job calibration method is a combination of test field calibration and actual object measurement. A portable test field is placed close to the object requiring measurement and is photographed together with the object. Self-calibration (Test field calibration) method utilizes a field with coordinated targets, images of this method field are taken from several positions and with different orientations, and the object and photo coordinates of the targets are used to derive the interior orientation parameters using bundle adjustment [40, 41].

3. Experimental Work

The experimental work of this study is carried out and achieved with calculations of interior orientation parameters (IOPs), exterior orientation parameters (EOPs), and object space (ground) coordinates of target points, which represent the main task of photogrammetry simultaneously (in one step) using bundle block adjustment method (BBA) based on collinearity equation to build and establish 3D real scale model. Also, the digital elevation model (DEM) and orthoimage are generated. Agisoft Metashape Professional program is used in the processing procedures.

This study will be implemented in four phases: data preparation and input phase, data processing phase, results (outputs) phase, and statistical analysis phase.

In the first phase, ground control points (GCPs) will establish, and the number of captured images will be selected. Then setting, the camera to acquire images, and images will be acquired. After that, loading images in the program, adding GCPs and CPs as markers in the Agisoft Metashape Professional program and inputting the ground coordinates of GCPs that will be used in data processing later.

In the data processing phase, the images will judge if they are inspected, and then the first step of building the 3D real scale model, aligning images, will be done. In images alignment, the interior orientation parameters (IOPs) and exterior orientation parameters (EOPs) will be determined, and object space coordinates of GCPs and CPs are also going to be calculated simultaneously (in one step) using the bundle block adjustment method (BBA) based on collinearity equation.

The establishment 3D real scale model, generation of a digital elevation model (DEM), and orthoimage building will be the final productions in this phase, which represent the results (outputs) in addition to the processing report.

On the other side of this study, the statistical analysis using the SPSS program will be performed to assess and evaluate the results by calculating residuals (errors) of GCPs and CPs. Root mean square error (RMSE), as well as standard error (δ), will be used in the study to validate the accuracy. The linear regression analysis of residuals is also will implement by scatter plot of residuals and finding the best fit line (BFL) for them. Also, the coefficient of determination (R^2) will be calculated. The following Figure 5 illustrates the four main phases of this paper in detail.

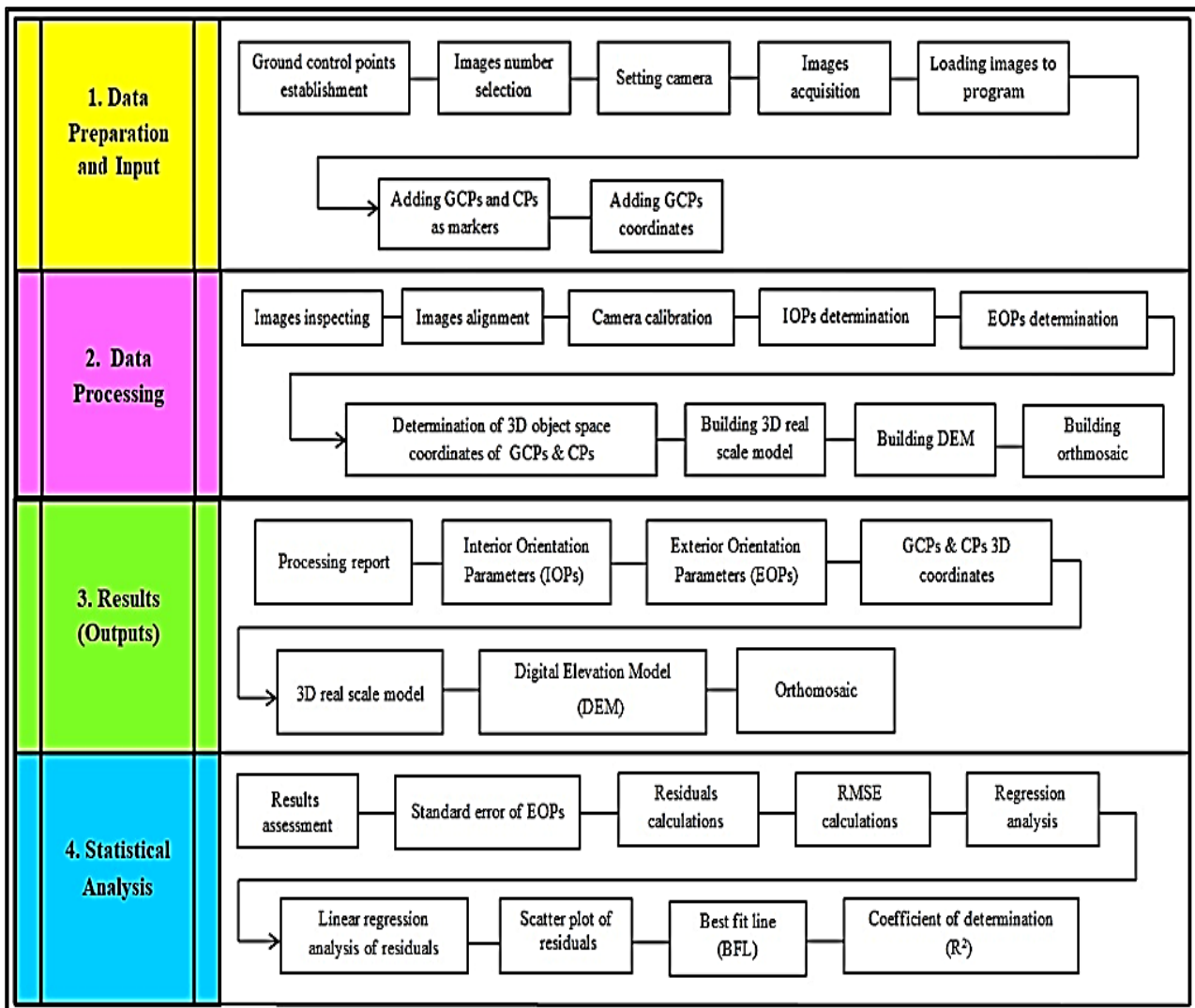


Figure 5: Experimental Work Phases (Data Preparation and Input, Data Processing, Results (Outputs), and Statistical Analysis)

Canon EOS 500D digital camera is used in this study to acquire 18 overlapped images (overlap percent g% for end lap is 35% while overlap percent g% for side lap is 65%); the technical characteristics of the camera are illustrated in Table 1, and the camera settings for capturing are 31mm focal length, 1600 ISO speed, 1/100 seconds shutter speed, manual exposure program, F5.6 aperture, 4752x3168 pixels image dimension (15.10 MP, large), JPG image format. The 18 digital images all cover the test field area that contains the targets. These images are taken in three strips. Each strip contains six images to form a block of images (1 block, 3 strips x 6 images = 18 images), as shown in Figure 6 below. The ground coordinates (object space coordinates) of targets are measured with the total station instrument (TOPCON GPT 3105N), as shown in Table 4 for ground control points (GCPs) coordinates and Table 5 for checkpoints (CPs) coordinates (measured X, Y, Z).

Table 1: Technical Characteristics of Canon 500D Digital Camera[42]

Item	Value
Type	Digital, single-lens reflex, AF / AE camera
Effective Pixels	Approx. 15.10 megapixels
Focal length (f)	18-55 mm
Image Sensor Size	22.3 x 14.9 mm
Recording pixels	Large: Approx. 15.10 megapixels (4752 x 3168) Medium: Approx. 8.00 megapixels (3456 x 2304) Small: Approx. 3.70 megapixels (2352 x 1568) RAW: Approx. 15.10 megapixels (4752 x 3168)
Focusing Modes	One-Shot AF, AI Servo AF, AI Focus AF, Manual focusing
Shutter Speeds	1/4000 sec. to 30 sec.
Image type	JPG, JPEG, RAW, RAW + JPEG simultaneous

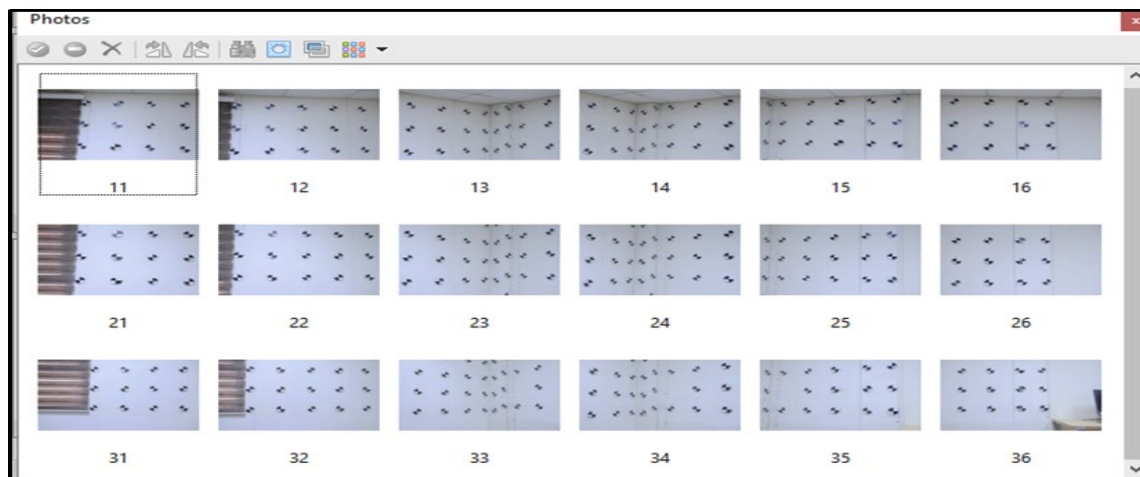


Figure 6: Block of 18 Images in 3 Strips

After capturing the images, they are loaded into the program, and all images are checked to see if there are inspected images or not. There are no inspected images (inspected images = 0). On the other hand, all images (18 images) are used in the modeling process. After loading and inspecting images, 90 artificial target points are added as markers in photos, see Figure 7, noting that the points with red colors are GCPs while the yellow points are CPs. The 3D object space coordinates of 25 points from 90 target points are added to the workspace of the program and used as ground control points (GCPs) (good distribution of GCPs is used in the edges and middle of the block) that are used in calculations process of building 3D real scale model while the remains of 65 points from 90 target points are used as checkpoints (CPs) to check the work; not used in calculations process (only for check).

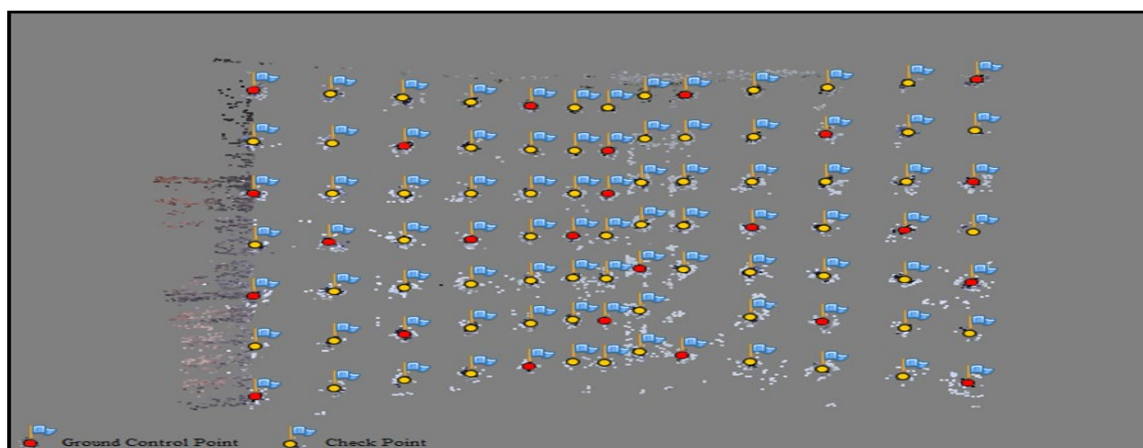


Figure 7: GCPs and CPs Number and Distribution

The next step is image alignment. In this step, the images are rearranged, organized, and aligned (see Figure 8). The images' alignment parameters are within high accuracy, and the alignment time is 5 sec. In image alignment, interior orientation parameters (IOPs) and exterior orientation parameters (EOPs) are calculated; also, 3D coordinates of the targets are calculated simultaneously. By using the available tools in the Agisoft Metashape Professional program, the 3D real-scale model can be built.

Finally, the digital products represented by the 3D real scale model, digital elevation model (DEM), and orthoimage are delivered.

4. Results and Statistical Analysis

4.1 Interior Orientation Parameters

calculations of interior orientation parameters (IOPs) of the camera are done to determine focal length f , principal point (C_x , C_y), radial distortion coefficient of 2nd, 4th, 6th, 8th -order, respectively, (K_1 , K_2 , K_3 , K_4), tangential distortion coefficient (P_1 , P_2 , P_3 , P_4), and affinity and skew coefficients (B_1 , B_2) through camera calibration process in photos alignment stage. The size of the images and pixel size are defined. See the following Table 2.

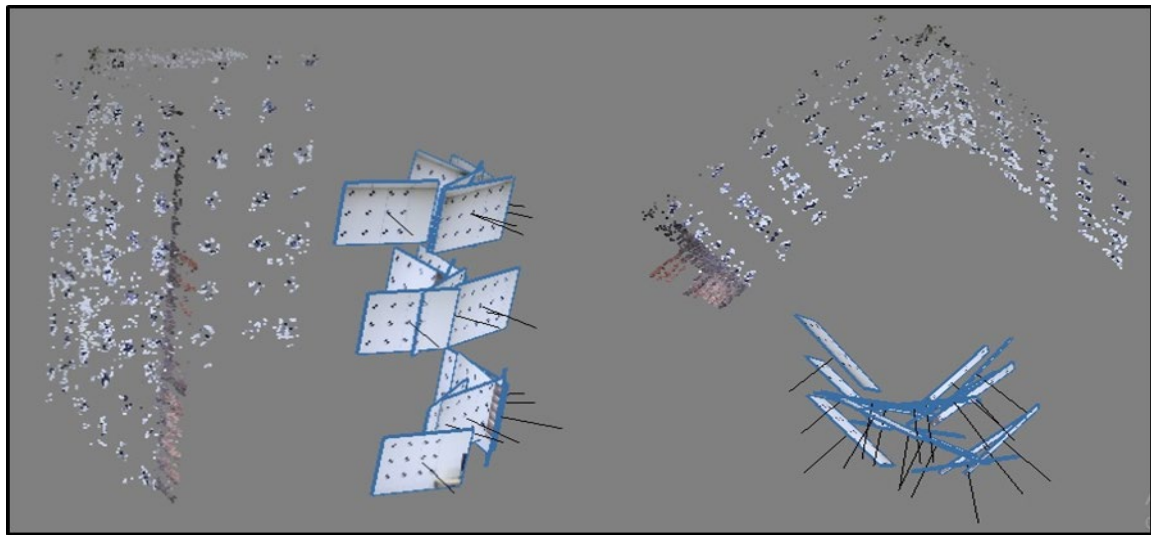


Figure 8: Images Alignment

Table 2: Interior Orientation Parameters (IOPs) of Camera

parameter	value	parameter	Value
f (pixel)	6503.71	B1	0
f (mm)	31	B2	0
C _x (pixel)	0	P1	0.0017415
C _y (pixel)	0	P2	0.00154896
K1	0.0205394	P3	0
K2	0.346983	P4	0
K3	0	Image Size (pixel)	4752 x 3168
K4	0	Pixel size (μ)	4.77 x 4.77

4.2 Exterior Orientation Parameters

Camera position (location) (X, Y, Z) and orientation (ω , ϕ , κ), which refer to exterior orientation parameters (EOPs) for all exposure stations (18 exposure stations), are calculated in the photos alignment step. The following Table 3 illustrates the cameras' exterior orientation parameters (EOPs).

Table 3: Exterior Orientation Parameters (EOPs) of Exposure Stations (cameras)

Exposure station	ID	X (m)	Y (m)	Z (m)	ω (deg.)	ϕ (deg.)	κ (deg.)
1	11	4.031363	1.278977	2.096736	97.988525	-29.500522	6.465244
2	12	3.802663	1.423642	2.135028	100.054062	-44.169184	6.446998
3	13	3.645188	1.729784	2.171874	111.123334	-71.548427	20.425288
4	14	3.609229	2.01412	2.195116	162.5566	-83.841791	73.912162
5	15	3.548386	2.093921	2.183008	-107.424199	-71.875081	164.512921
6	16	3.904953	2.458451	2.182324	-100.484746	-50.694927	171.431156
7	21	3.996275	1.448141	1.574741	94.537026	-33.218206	3.43942
8	22	3.911445	1.345189	1.578039	93.623072	-40.024939	2.495859
9	23	3.696048	1.730142	1.599033	102.101048	-72.001484	12.340423
10	24	3.612275	2.030948	1.641277	158.952344	-86.607741	70.392834
11	25	3.498316	1.874795	1.6265	-109.017587	-76.870295	161.996576
12	26	3.722216	2.452755	1.633921	-99.057317	-53.36615	172.110075
13	31	3.754209	1.136995	0.918363	93.375863	-32.338316	2.328227
14	32	3.646026	1.27624	0.939225	93.728783	-42.650872	1.976873
15	33	3.418603	1.484831	0.919605	101.635954	-68.724438	10.908633
16	34	3.537484	1.954715	0.9724	139.713358	-85.062827	50.178552
17	35	3.489241	1.87981	0.957539	-111.347839	-76.725478	159.542673
18	36	3.525061	2.525454	0.909552	-99.080928	-54.579977	171.492968

4.3 Three Dimensional (3D) Ground Coordinates of Real Scale Model

The three-dimensional (3D) object space coordinates (ground coordinates) of all artificial target points (90 target points) are calculated. Twenty-five points of target points were used as ground control points utilized in the calculations of 3D coordinates

of the model, and 65 of them were used as checkpoints to check the work, with an accuracy of 0.005 m for all points, see Table 4 for GCPs 3D coordinates, and Table 5 for CPs 3D coordinates (calculated X, Y, Z).

Table 4: Calculated and Measured Ground Coordinates of GCPs and Residuals

Point	ID	Calculated			Measured			Residuals		
		X (m)	Y (m)	Z (m)	X (m)	Y (m)	Z (m)	V _x (m)	V _y (m)	V _z (m)
GCP1	1A	4.758827	3.17317	2.632633	4.7585	3.175	2.633	0.000327	-0.00183	-0.000367
GCP2	1E	5.751926	2.512856	2.63085	5.7565	2.514	2.633	-0.004574	-0.001144	-0.00215
GCP3	1I	5.894757	1.980962	2.708215	5.896	1.9805	2.71	-0.001243	0.000462	-0.001785
GCP4	1M	5.270338	1.032081	2.710184	5.2685	1.032	2.71	0.001838	8.1E-05	0.000184
GCP5	2C	5.254007	2.841143	2.333137	5.254	2.8415	2.3335	7E-06	-0.000357	-0.000363
GCP6	2G	5.938088	2.262581	2.332534	5.9385	2.263	2.334	-0.000412	-0.000419	-0.001466
GCP7	2K	5.556367	1.480568	2.412656	5.5565	1.4805	2.413	-0.000133	6.8E-05	-0.000344
GCP8	3A	4.7544	3.173558	2.03445	4.755	3.173	2.0335	-0.0006	0.000558	0.00095
GCP9	3G	5.936642	2.26357	2.030094	5.937	2.2635	2.0305	-0.000358	7E-05	-0.000406
GCP10	3M	5.26654	1.03141	2.111336	5.264	1.0325	2.111	0.00254	-0.00109	0.000336
GCP11	4B	5.004601	3.002265	1.736003	5.002	3.002	1.733	0.002601	0.000265	0.003003
GCP12	4D	5.49974	2.670107	1.730854	5.501	2.671	1.731	-0.00126	-0.000893	-0.000146
GCP13	4F	5.942183	2.386303	1.732045	5.946	2.387	1.7325	-0.003817	-0.000697	-0.000455
GCP14	4J	5.718728	1.726747	1.813251	5.719	1.7265	1.813	-0.000272	0.000247	0.000251
GCP15	4L	5.392159	1.22432	1.812671	5.3905	1.2255	1.812	0.001659	-0.00118	0.000671
GCP16	5A	4.75283	3.173894	1.435753	4.752	3.171	1.435	0.00083	0.002894	0.000753
GCP17	5H	5.916831	2.136396	1.511852	5.9215	2.137	1.512	-0.004669	-0.000604	-0.000148
GCP18	5M	5.261427	1.02813	1.513087	5.2595	1.0305	1.513	0.001927	-0.00237	8.7E-05
GCP19	6C	5.251969	2.83923	1.134771	5.2525	2.8405	1.1345	-0.000531	-0.00127	0.000271
GCP20	6G	5.933172	2.26542	1.133428	5.934	2.266	1.1325	-0.000828	-0.00058	0.000928
GCP21	6K	5.545402	1.476367	1.216128	5.5445	1.4775	1.2155	0.000902	-0.001133	0.000628
GCP22	7A	4.752618	3.171058	0.834913	4.752	3.17	0.8355	0.000618	0.001058	-0.000587
GCP23	7E	5.751752	2.51177	0.835109	5.7535	2.5135	0.834	-0.001748	-0.00173	0.001109
GCP24	7I	5.874538	1.973693	0.912858	5.8745	1.974	0.912	3.8E-05	-0.000307	0.000858
GCP25	7M	5.257711	1.028363	0.911953	5.2555	1.031	0.913	0.002211	-0.002637	-0.001047

4.4 Real Scale Model, DEM, and Orthoimage

The model texture building stage is interested in building the texture based on the original images and mesh to reach the real object (real scale model). Where the images are combined into a texture map and wrapped around the mesh to produce the original object. Generic mode is used in mapping with 4096 x 1 texture size/ count and enabled hole filling and ghosting filter. The blending mode is mosaic (default). The time for UV mapping is 39 seconds, and the blending time is 1 minute and 45 seconds, see Figure 9.

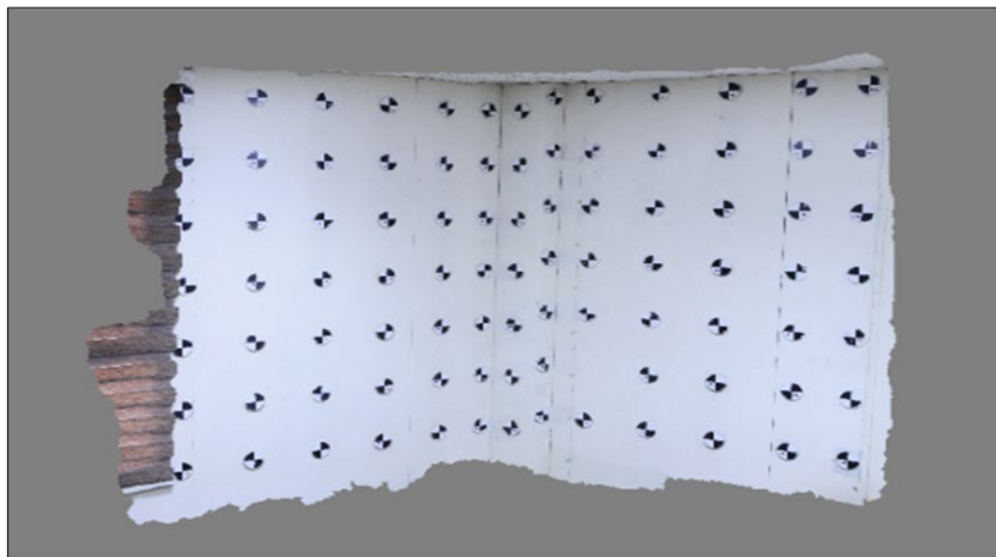


Figure 9: Three Dimensional (3D) Real Scale Model

Table 5: Calculated and Measured Ground Coordinates of CPs and Residuals

Point	ID	Calculated			Measured			Residuals		
		X (m)	Y (m)	Z (m)	X (m)	Y (m)	Z (m)	V _x (m)	V _y (m)	V _z (m)
CP1	1B	5.005035	3.00616	2.63411	5.003	3.0045	2.634	0.002035	0.00166	0.00011
CP2	1C	5.254059	2.842546	2.633931	5.2555	2.844	2.635	-0.001441	-0.001454	-0.001069
CP3	1D	5.499126	2.673442	2.631057	5.5005	2.675	2.6325	-0.001374	-0.001558	-0.001443
CP4	1F	5.945819	2.387	2.632588	5.949	2.388	2.635	-0.003181	-0.001	-0.002412
CP5	1G	5.939083	2.261986	2.629659	5.9405	2.2625	2.632	-0.001417	-0.000514	-0.002341
CP6	1H	5.928292	2.708081	2.130912	5.933	2.709	2.131	-0.004708	-0.000919	-8.8E-05
CP7	1J	5.728365	1.730322	2.711002	5.7285	1.7295	2.71	-0.000135	0.000822	0.001002
CP8	1K	5.558111	1.481668	2.708191	5.5575	1.4805	2.708	0.000611	0.001168	0.000191
CP9	1L	5.397974	1.227497	2.709919	5.3975	1.227	2.71	0.000474	0.000497	-8.1E-05
CP10	2A	4.756181	3.174998	2.334715	4.757	3.1745	2.334	-0.000819	0.000498	0.000715
CP11	2B	5.00408	3.004317	2.334992	5.0045	3.0035	2.335	-0.00042	0.000817	-8E-06
CP12	2D	5.499071	2.672468	2.333699	5.501	2.6735	2.335	-0.001929	-0.001032	-0.001301
CP13	2E	5.752131	2.51273	2.331717	5.755	2.513	2.333	-0.002869	-0.00027	-0.001283
CP14	2F	5.947346	2.386684	2.332951	5.9495	2.387	2.335	-0.002154	-0.000316	-0.002049
CP15	2H	5.930913	2.12973	2.413075	5.933	2.13	2.415	-0.002087	-0.00027	-0.001925
CP16	2I	5.890499	1.979866	2.412498	5.891	1.979	2.414	-0.000501	0.000866	-0.001502
CP17	2J	5.725238	1.728297	2.409837	5.725	1.7275	2.41	0.000238	0.000797	-0.000163
CP18	2L	5.396273	1.227178	2.41203	5.3955	1.227	2.412	0.000773	0.000178	3E-05
CP19	2M	5.268425	1.03248	2.412593	5.267	1.033	2.412	0.001425	-0.00052	0.000593
CP20	3B	5.000807	3.002159	2.03432	5.001	3.003	2.034	-0.000193	-0.000841	0.00032
CP21	3C	5.252166	2.83943	2.034545	5.2545	2.841	2.034	-0.002334	-0.00157	0.000545
CP22	3D	5.498258	2.670972	2.033519	5.501	2.6725	2.034	-0.002742	-0.001528	-0.000481
CP23	3E	5.750829	2.512292	2.032179	5.753	2.5125	2.033	-0.002171	-0.000208	-0.000821
CP24	3F	5.941863	2.387105	2.032124	5.945	2.388	2.033	-0.003137	-0.000895	-0.000876
CP25	3H	5.921896	2.134444	2.110411	5.926	2.135	2.1115	-0.004104	-0.000556	-0.001089
CP26	3I	5.885349	1.978751	2.111973	5.8865	1.978	2.1125	-0.001151	0.000751	-0.000527
CP27	3J	5.722021	1.728386	2.111144	5.722	1.728	2.111	2.1E-05	0.000386	0.000144
CP28	3K	5.552835	1.478996	2.113887	5.551	1.479	2.113	0.001835	-4E-06	0.000887
CP29	3L	5.393402	1.22552	2.11288	5.392	1.226	2.1125	0.001402	-0.00048	0.00038
CP30	4A	4.75081	3.167134	1.734104	4.754	3.172	1.7335	-0.00319	-0.004866	0.000604
CP31	4C	5.251332	2.840141	1.734325	5.251	2.841	1.734	0.000332	-0.000859	0.000325
CP32	4E	5.749449	2.512463	1.733542	5.753	2.513	1.7335	-0.003551	-0.000537	4.2E-05
CP33	4G	5.934625	2.263125	1.735263	5.937	2.264	1.736	-0.002375	-0.000875	-0.000737
CP34	4H	5.921103	2.134669	1.815176	5.925	2.135	1.816	-0.003897	-0.000331	-0.000824
CP35	4I	5.883021	2.977615	1.811436	5.883	2.977	1.812	2.1E-05	0.000615	-0.000564
CP36	4K	5.550926	1.477943	1.813902	5.551	1.4785	1.8135	-7.4E-05	-0.000557	0.000402
CP37	4M	5.263952	1.029221	1.815762	5.262	1.0305	1.815	0.001952	-0.001279	0.000762
CP38	5B	5.001316	3.00207	1.434971	5.0025	3.002	1.434	-0.001184	7E-05	0.000971
CP39	5C	5.251534	2.839038	1.43442	5.252	2.84	1.434	-0.000466	-0.000962	0.00042
CP40	5D	5.497761	2.669986	1.433363	5.4995	2.6715	1.433	-0.001739	-0.001514	0.000363
CP41	5E	5.750052	2.510841	1.433512	5.754	2.512	1.433	-0.003948	-0.001159	0.000512
CP42	5F	5.939973	2.386225	1.43274	5.945	2.388	1.433	-0.005027	-0.001775	-0.00026
CP43	5G	5.931131	2.263015	1.432015	5.935	2.264	1.432	-0.003869	-0.000985	1.5E-05
CP44	5I	5.879488	1.976191	1.511984	5.882	1.9765	1.512	-0.002512	-0.000309	-1.6E-05
CP45	5J	5.715181	1.725519	1.512148	5.716	1.7255	1.512	-0.000819	1.9E-05	0.000148
CP46	5K	5.54623	1.476554	1.512053	5.547	1.477	1.512	-0.00077	-0.000446	5.3E-05
CP47	5L	5.386776	1.221463	1.513477	5.386	1.2225	1.5135	0.000776	-0.001037	-2.3E-05
CP48	6A	4.753178	3.173315	1.134023	4.752	3.1705	1.134	0.001178	0.002815	2.3E-05
CP49	6B	5.003008	3.001799	1.132554	5.001	3.0005	1.132	0.002008	0.001299	0.000554
CP50	6D	5.499888	2.670084	1.138505	5.5005	2.6715	1.138	-0.000612	-0.001416	0.000505
CP51	6E	5.752342	2.509906	1.134717	5.755	2.512	1.134	-0.002658	-0.002094	0.000717
CP52	6F	5.940534	2.385683	1.134459	5.9445	2.387	1.1335	-0.003966	-0.001317	0.000959
CP53	6H	5.916458	2.137165	1.211793	5.9205	2.138	1.211	-0.004042	-0.000835	0.000793
CP54	6J	5.713362	1.723715	1.211704	5.714	1.7245	1.211	-0.000638	-0.000785	0.000704
CP55	6L	5.384994	1.219401	1.215307	5.383	1.221	1.215	0.001994	-0.001599	0.000307
CP56	6M	5.259264	1.029358	1.210865	5.2585	1.0315	1.2105	0.000764	-0.002142	0.000365
CP57	7B	5.000531	3.002089	0.836316	5.0005	3.0015	0.8365	3.1E-05	0.000589	-0.000184
CP58	7C	5.251219	2.838699	0.835557	5.252	2.841	0.835	-0.000781	-0.002301	0.000557
CP59	7D	5.498665	2.669999	0.835576	5.5005	2.672	0.835	-0.001835	-0.002001	0.000576
CP60	7F	5.940958	2.385732	0.836351	5.944	2.387	0.835	-0.003042	-0.001268	0.001351
CP61	7G	5.929506	2.262497	0.836262	5.9265	2.263	0.835	0.003006	-0.000503	0.001262
CP62	7H	5.916881	2.135705	0.919431	5.9215	2.137	0.918	-0.004619	-0.001295	0.001431
CP63	7J	5.711688	1.724482	0.911594	5.711	1.725	0.911	0.000688	-0.000518	0.000594
CP64	7K	5.543471	1.473652	0.91348	5.5415	1.4745	0.913	0.001971	-0.000848	0.00048
CP65	7L	5.38387	1.220841	0.911504	5.3825	1.2225	0.912	0.00137	-0.001659	-0.000496

The Digital elevation model (DEM) is a surface represented as a regular grid, with height values stored in each grid cell. DEM can be generated from a sparse point cloud, dense point cloud, mesh, or directly from depth maps. The source data used for DEM production is meshed with the local (m) coordinate system and planar projection type and enabled interpolation. The size of DEM is 4867 x 4362 pixels. The processing time for DEM production is 9 seconds. See Figure 10 below.

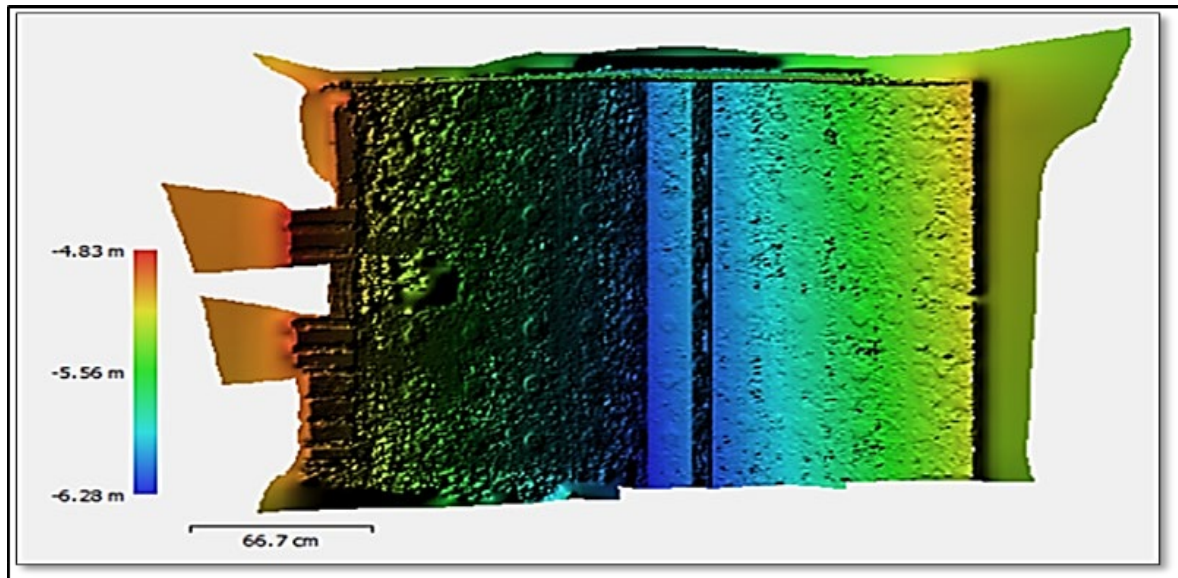


Figure 10: Digital Elevation Model (DEM)

orthoimage (orthomosaic) is a combined image created by merging the original images projected on the object's surface and transforming them into the selected projection. A polygonal model (mesh) or DEM can be used as a surface where images are projected. The mesh is used as a surface. The orthoimage size is 6151 x 5613 pixels with planar projection and the local (m) coordinate system. See Figure 11 below. Hole filling is enabled with the mosaic blending mode. Colors are 3 bands, unit 8, and the time for orthoimage reconstruction is 23 seconds.

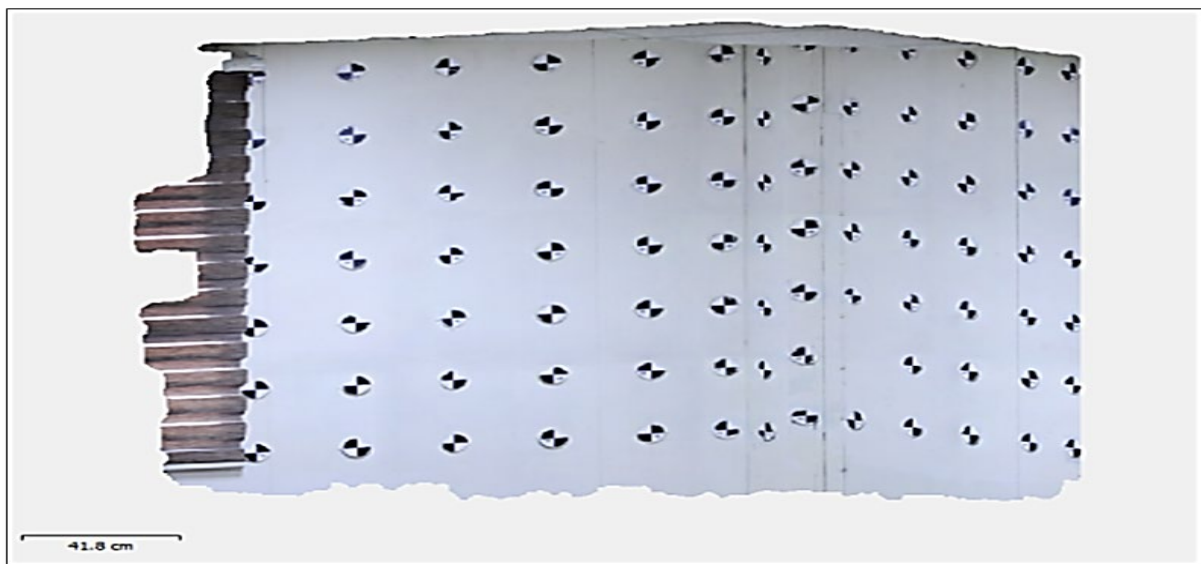


Figure 11: Orthoimage

4.5 Statistical Analysis

Statistical analysis is used in this paper to analyze and assess the results obtained from the calculations process by using specific statistical parameters, including root mean square error (RMSE), residuals (errors), and standard error (δ). Linear regression analysis is also used to analyze the residuals by scatter plot and best fit line (BFL) [43, 44]. SPSS program is used in the analysis. Table 6 gives a statistical analysis summary of the results. Residuals and RMSE are calculated by comparing the calculated object space coordinates of GCPs and CPs of 90 artificial targets and the measured object space coordinates of GCPs and CPs. Residuals in the X-direction, Y-direction, and Z-direction are calculated by using Equations 8, 9, and 10, respectively [45, 46] and illustrated in Table 4 (for GCPs) and Table 5 (for CPs). The scatter plot of residuals and their BFL in X-Y-Z-

directions are illustrated in Figure 12 for GCPs and CPs. Also, the coefficient of determination (R^2), see Equation 11 [47], is determined and illustrated in Table 7. while RMSE in X-direction, Y-direction, Z-direction (vertical RMSE), horizontal RMSE, and total RMSE is calculated by using Equations 12, 13, 14, 15, 16 respectively, for GCPs and CPs [11, 48] and given in Table 8, Figure 13(a) illustrates RMSE. The standard error of EOPs, see Equation 17 [49], is given in the Agisoft program and given in Table 9. The standard error of X, Y, Z (position), and ω, ϕ, κ (rotation) are illustrated in Figure 13 (b) and (c), respectively.

Table 6: Summary of Statistical Analysis

parameter	Value	
	Max.	Min.
V_x - GCPs (m)	0.004669	7.00E-06
V_y - GCPs (m)	0.002894	6.80E-05
V_z - GCPs (m)	0.003003	8.70E-05
V_x - CPs (m)	0.005027	2.10E-05
V_y - CPs (m)	0.004866	4.00E-06
V_z - CPs (m)	0.002412	8.00E-06
δx -ES (m)	± 0.001083	± 0.000784
δy -ES (m)	± 0.001173	± 0.000881
δz -ES (m)	± 0.001317	± 0.000978
$\delta \omega$ -ES (degree)	± 0.474	± 0.01
$\delta \phi$ -ES (degree)	± 0.032	± 0.028
$\delta \kappa$ -ES (degree)	± 0.473	± 0.037

$$V_x = X_c - X_m \tag{8}$$

$$V_y = Y_c - Y_m \tag{9}$$

$$V_z = Z_c - Z_m \tag{10}$$

Where V_x, V_y, V_z are (residual) in X-Y-Z directions (m), respectively, X_c, Y_c, Z_c are calculated to ground coordinates of X-Y-Z directions (m), respectively, X_m, Y_m, Z_m are measured ground coordinates of X-Y-Z directions (m), respectively

$$R^2 = 1 - \frac{SS_{Res}}{SS_{Tot}} \tag{11}$$

Where R^2 is the coefficient of determination, SS_{Res} is the residual sum of squares, and SS_{Tot} is the total sum of squares.

$$(RMSE)_X = \sqrt{\frac{\sum(X_c - X_m)^2}{N_i}} \tag{12}$$

$$(RMSE)_Y = \sqrt{\frac{\sum(Y_c - Y_m)^2}{N_i}} \tag{13}$$

$$(RMSE)_Z = \sqrt{\frac{\sum(Z_c - Z_m)^2}{N_i}} \tag{14}$$

$$(RMSE)_{XY} = \sqrt{(RMSE)_X^2 + (RMSE)_Y^2} \tag{15}$$

$$(RMSE)_{xyz} = \sqrt{(RMSE)_X^2 + (RMSE)_Y^2 + (RMSE)_Z^2} \tag{16}$$

Where X_c, Y_c, Z_c are calculated to ground coordinates of X-Y-Z directions (m), respectively, $X_m, Y_m,$ and Z_m are measured as ground coordinates of X-Y-Z directions (m), respectively. $(RMSE)_X, (RMSE)_Y, (RMSE)_Z$ are root mean square errors in X-Y-Z directions (m), respectively. $(RMSE)_{XY}$ is the horizontal root mean square error (m). $(RMSE)_{xyz}$ is the total root mean square error (m), and N_i is the number of points.

$$SE(\delta) = \frac{SD}{\sqrt{N_i}} \tag{17}$$

SE is the standard error, SD is the standard deviation, and N_i is the number of points.

Table 7: R- squared Values of Residuals

Error	R2					
	X	Y	Z	X	Y	Z
Point type	GCPs	GCPs	GCPs	CPs	CPs	CPs
R-squared value (R2)	0.019	0.031	0.138	0.008	0.084	0.311

Table 8: Root Mean Square Error (RMSE) of GCPs and CPs

Analysis with respect to	Type of points	
	Ground control points (GCPs)	Checkpoints (CPs)
Number of points	25	65
RMSE-X (m)	± 0.001950772	± 0.002269255
RMSE-Y (m)	± 0.001236879	± 0.001266661
RMSE-XY (Horizontal) (m)	± 0.002309845	± 0.002598836
RMSE-Z (Vertical) (m)	± 0.001032447	± 0.000869544
RMSE-XYZ (Total) (m)	± 0.002530085	± 0.002740448

Table 9: Standard Error of Exposure Stations (Cameras)

Exposure Station	ID	δx (m)	δy (m)	δz (m)	$\delta \omega$ (deg.)	$\delta \phi$ (deg.)	$\delta \kappa$ (deg.)
1	11	± 0.00085	± 0.000906	± 0.001039	± 0.033	± 0.029	± 0.037
2	12	± 0.000862	± 0.000977	± 0.00111	± 0.042	± 0.028	± 0.044
3	13	± 0.000859	± 0.001009	± 0.001137	± 0.01	± 0.029	± 0.098
4	14	± 0.000851	± 0.001013	± 0.001127	± 0.261	± 0.032	± 0.26
5	15	± 0.000869	± 0.001033	± 0.001152	± 0.097	± 0.028	± 0.103
6	16	± 0.000784	± 0.000904	± 0.000978	± 0.044	± 0.028	± 0.051
7	21	± 0.000797	± 0.000881	± 0.001011	± 0.035	± 0.028	± 0.038
8	22	± 0.000839	± 0.000926	± 0.001072	± 0.039	± 0.028	± 0.042
9	23	± 0.000822	± 0.000973	± 0.0011	± 0.103	± 0.028	± 0.102
10	24	± 0.000819	± 0.000996	± 0.001111	± 0.474	± 0.032	± 0.473
11	25	± 0.000872	± 0.001038	± 0.001181	± 0.135	± 0.028	± 0.14
12	26	± 0.000806	± 0.000963	± 0.001061	± 0.047	± 0.028	± 0.054
13	31	± 0.001083	± 0.00111	± 0.001281	± 0.036	± 0.029	± 0.038
14	32	± 0.001044	± 0.001113	± 0.001258	± 0.042	± 0.029	± 0.043
15	33	± 0.001066	± 0.001173	± 0.001317	± 0.088	± 0.029	± 0.087
16	34	± 0.000959	± 0.001087	± 0.001197	± 0.339	± 0.031	± 0.337
17	35	± 0.000985	± 0.001098	± 0.001227	± 0.134	± 0.028	± 0.138
18	36	± 0.001008	± 0.001136	± 0.001267	± 0.052	± 0.029	± 0.058

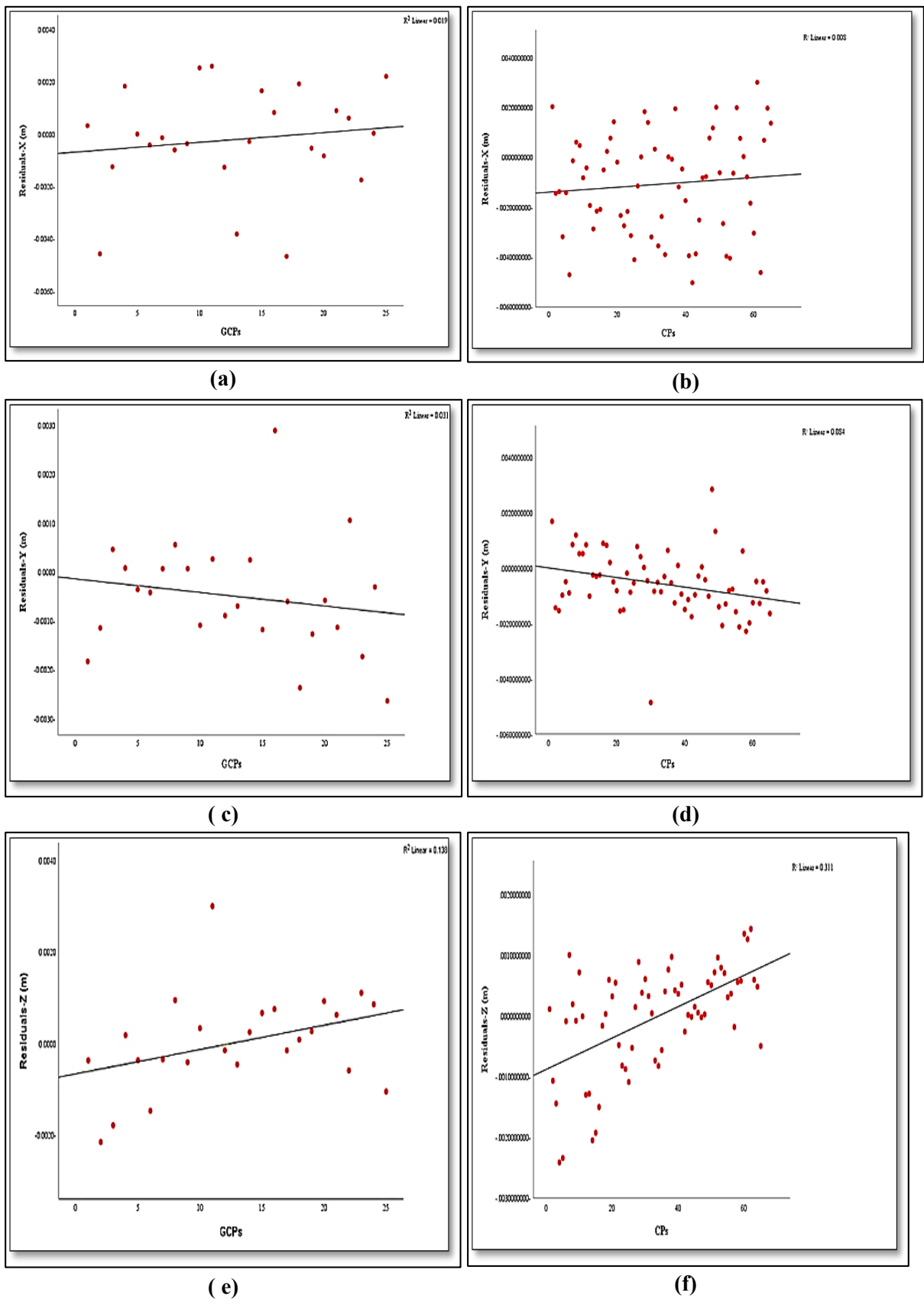
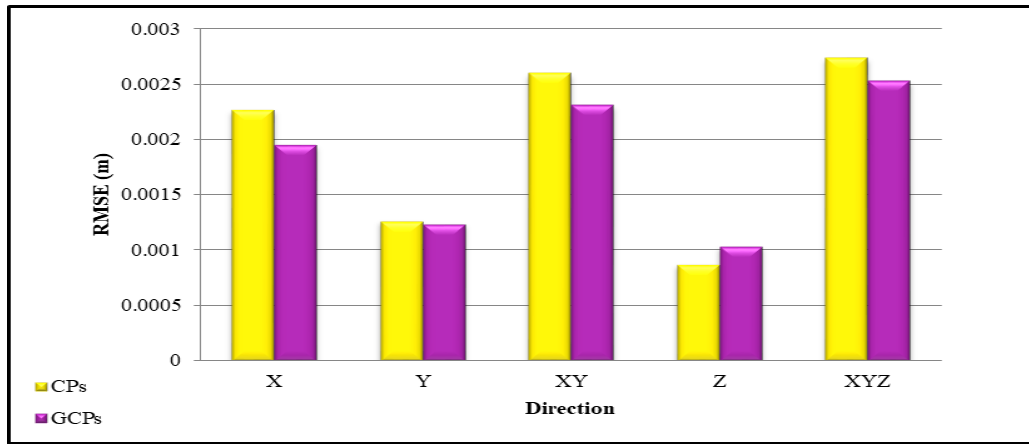
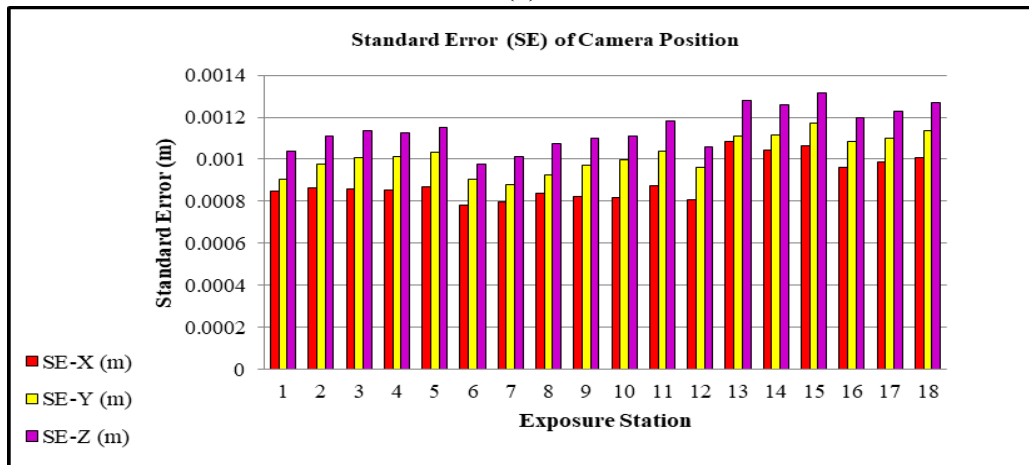


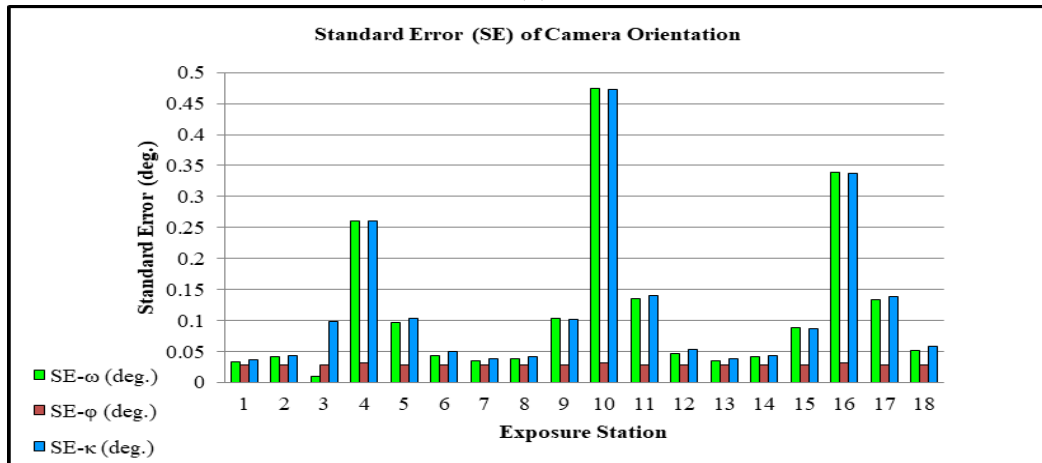
Figure 12: Scatter Plot and Best Fit Line of (a) X-direction for GCPs (b) X-direction for CPs (c) Y-direction for GCPs (d) Y-direction for GCPs (e) Z-direction for GCPs (f) Z-direction for CPs



(a)



(b)



(c)

Figure 13: Statistical Analysis (a) Root Mean Square Error (RMSE) of GCPs and CPs (b) Standard Error for Exposure Stations Position (c) Standard Error for Exposure Stations Orientation

4.6 Discussion

Generally, this paper includes two aspects. Firstly, the Determination of interior orientation parameters (IOPs), exterior orientation parameters (EOPs), and object space (ground) coordinates (X-Y-Z) simultaneously using the bundle block adjustment method based on collinearity equation. These elements represent the core of photogrammetry to establish a 3D real scale model. The second aspect is the assessment and evaluation of results through statistical analysis, including particular statistical parameters; residuals (errors), root mean square error (RMSE), standard error (δ), and linear regression analysis (LRA).

Table 2 illustrates the camera's interior orientation parameters (IOPs), which are calculated in the camera calibration process. Also, exterior orientation parameters (EOPs) are calculated and illustrated in Table 3. The ground coordinates of all 90 target points are calculated and illustrated in Table 4 (for GCPs) and Table 5 (for CPs). The statistical analysis of the results shows that the maximum error in the X-direction is 0.004669 m for GCPs (GCP17) and 0.005027 m for CPs (CP42), the maximum error in

Y-direction is 0.002894 m for GCPs (GCP16) and 0.004866 m for CPs (CP30) and the maximum error in Z-direction is 0.003003 m for GCPs (GCP11) and 0.002412 m for CPs (CP4). While the minimum error in the X-direction is 7.00E-06 m for GCPs (GCP5) and 2.10E-05 m for CPs (CP35), the minimum error in Y-direction is 6.80E-05m for GCPs (GCP7) and 4.00E-06 m for CPs (CP28), and the minimum error in Z-direction is 8.70E-05 m for GCPs (GCP18) and 8.00E-06 m for CPs (CP11). The linear regression analysis is performed to analyze the residuals (errors) by scatter plot of them and find the best fit line (BFL); also, the coefficient of determination (R^2) is calculated. R^2 values for GCPs are 0.019, 0.031, 0.138 in X, Y, Z directions, respectively. R^2 values for CPs are 0.008 (minimum), 0.084, 0.311 (maximum) in X, Y, Z directions, respectively. The scatter plot of GCPs residuals, and CPs residuals showed a homogeneity where the scatter plot of both GCPs and CPs, in X and Z directions up to the right (Fig 12 (a), (b), (e), (f)) and the scatter plot of them in the Y direction down to the right (Fig 12 (c), (d)). The RMSE is calculated and analyzed for GCPs and CPs. for GCPs, the RMSE-X is ± 0.001950772 m, RMSE-Y is ± 0.001236879 m, the horizontal root mean square error (RMSE-XY) is ± 0.002309845 m, the vertical root mean square error (RMSE-Z) is ± 0.001032447 m. The total root mean square error (RMSE-XYZ) is ± 0.002530085 m. for CPs, the RMSE-X is ± 0.002269255 m, RMSE-Y is ± 0.001266661 m, the horizontal root means square error (RMSE-XY) is ± 0.002598836 m, the vertical root means square error (RMSE-Z) is ± 0.000869544 m, and the total root mean square error (RMSE-XYZ) is ± 0.002740448 m. In general, the RMSE of CPs is higher than the RMSE of GCPs in all directions except the Z- the direction where the RMSE of GCPs is higher than the RMSE of CPs. The standard error (δ) of EOPs of exposure stations are illustrated in Table 9, the maximum values are ± 0.001083 m (exposure station 31), ± 0.001173 m (exposure station 33), ± 0.001317 m (exposure station 33), ± 0.474 deg. (exposure station 24), ± 0.032 deg. (exposure stations 14 and 24), ± 0.473 deg. (exposure station 24) for x, y, z, ω , ϕ , κ , respectively. And the minimum values are ± 0.000784 m (exposure station 16), ± 0.000881 m (exposure station 21), ± 0.000978 m (exposure station 16), ± 0.01 deg. (exposure station 13), ± 0.028 deg. (exposure stations 12, 15, 16, 21, 22, 23, 25, 26, and 35), ± 0.037 deg. (exposure station 11) for x, y, z, ω , ϕ , κ , respectively. Generally, exposure stations 14, 24, and 34 showed the maximum standard error in ω , ϕ , κ orientation angles, respectively. The figure of the standard error of exposure stations position, Figure 13 (b), showed that the standard error in its highest values in the Z- direction followed by Y- direction, and then the error in the X- the direction in its minimum values in all exposure stations.

5. Conclusion

The 3D real-scale models have an important role in many daily life applications. This study is implemented to achieve the main task, which is the establishment of the 3D real scale model through photogrammetric processes, including the determination of IOPs, EOPs, and 3D coordinates of the target points of the model. Based on the collinearity equation, the process is performed using the bundle block adjustment method (BBA), which is considered an important processing step for deriving high-quality and accurate 3D models, DEM, and orthoimage. The block of 18 images with 3 strips, each with 6 images, is used in this work. The final results are with high accuracy for determining the EOPs and IOPs, and 3D coordinates of the model. The number and distribution of GCPs is also an important factor affecting estimates and calculations' accuracy. As well known, the small number of GCPs may lead to lower accuracy. Also, a good distribution of the GCPs would lead to better estimates and vice versa. In general, the calculated IOPs, EOPs, and 3D coordinates of the real scale model are within a reliable accuracy when the overall accuracy of calculations is 0.005 m. The total RMSE (RMSE_{xyz}) of GCPs is ± 2.530085 mm, while the total RMSE (RMSE_{xyz}) of CPs is ± 2.740448 mm.

Author contribution

All authors contributed equally to this work.

Funding

This research received no specific grant from any funding agency in the public, commercial, or not-for-profit sectors.

Data availability statement

The data that support the findings of this study are available on request from the corresponding author.

Conflicts of interest

The authors declare that there is no conflict of interest.

References

- [1] A. Goktepe and E. Kocaman, Analysis of camera calibrations using direct linear transformation and bundle adjustment methods, *Sci. Res. Essays.*, 5 (2010) 869–872.
- [2] Z. DURAN and M. E. ATİK, Accuracy comparison of interior orientation parameters from different photogrammetric software and direct linear transformation method, *Int. J. Eng. Geosci.*, 6 (2021) 74–80. <https://doi.org/10.26833/ijeg.691696>
- [3] P. Kozikowski, Extracting Three-dimensional Information from SEM Images by Means of Photogrammetry, *Micron*, 134 (2020) 102873. <https://doi.org/10.1016/j.micron.2020.102873>
- [4] E. Stylianidis, P. Patias, V. Tsioukas, L. Sechidis, and C. Georgiadis, a Digital Close-Range Photogrammetric Technique for Monitoring Slope Displacements, *Proc. of 11th FIG Symp. Deform. Meas. Santorini, Greece, 2003.*

- [5] M. H. M. Room and A. Ahmad, Mapping of a river using close range photogrammetry technique and unmanned aerial vehicle system, *IOP Conf. Ser. Earth Environ. Sci.*, 18 (2014).
- [6] C. Fraser and H. Hanley, Developments in Close-Range Photogrammetry for 3D Modelling: the iWitness Example, *Process. Vis. using High-Resolution Imag.*, 4 (2004) 18–20
- [7] A. Jebur, F. Abed, and M. Mohammed, Assessing the performance of commercial Agisoft PhotoScan software to deliver reliable data for accurate 3D modelling, *MATEC Web Conf.*, 162 (2018) 11. <https://doi.org/10.1051/mateconf/201816203022>
- [8] A. Z. Khalaf, A. Hameed, G. Branch, and G. Branch, Orthomosaic from Generating 3D Models with Photogrammetry, *Int. j. innov. sci. res. technol.*, 5 (2020) 48–60. <https://www.ijisrt.com/assets/upload/files/IJISRT20MAR109.pdf>
- [9] A. A. Belmonte, M. M. P. Biong, and E. G. Macatulad, DEM generation from close-range photogrammetry using extended python photogrammetry toolbox, *Int. Arch. Photogramm. Remote Sens. Spat. Inf. Sci. - ISPRS Arch.*, 42 (2013) 11–19. <https://doi.org/10.5194/isprs-archives-XLII-4-W5-11-2017>
- [10] J. Timur, Accuracy of DSM By Using Unmanned Aerial Vehicles on the Downstream of Welang Riverbank, District of Pasuruan, Jawa Timur, 2021. <http://dx.doi.org/10.30737/ukarst>
- [11] S. I. Jiménez-Jiménez, W. Ojeda-Bustamante, M. D. J. Marcial-Pablo, and J. Enciso, Digital terrain models generated with low-cost UAV photogrammetry: Methodology and accuracy, *ISPRS Int. J. Geo-Information.*, 10 (2021). <https://doi.org/10.3390/ijgi10050285>
- [12] J. Hu, E. Liu, and J. Yu, Application of Structural Deformation Monitoring Based on Close-Range Photogrammetry Technology, *Adv. Civ. Eng.*, 2021 (2021). <https://doi.org/10.1155/2021/6621440>
- [13] C. Fraser, S. Cronk, and H. Hanley, Close-range photogrammetry in traffic incident management, *Int. Arch. Photogramm. Remote Sens. Spat. Inf. Sci. - ISPRS Arch.*, 37 (2008) 125–128.
- [14] G. Zhao, C. Zhang, X. Jing, X. Ling, and S. Chen, Study on the Technologies of Close Range Photogrammetry and Applications in the Manufacture of Aviation, *Adv. Eng. Res.*, 164 (2018) 480–487. <https://doi.org/10.2991/icmse-18.2018.91>
- [15] W. YiMeng, Y. ShuYue, R. Shuai, C. Shuai, and L. JingZhun, Close-range industrial photogrammetry and application: review and outlook, 2020. <https://doi.org/10.1117/12.2576470>
- [16] P. Burdziakowski and P. Tysiac, Combined close range photogrammetry and terrestrial laser scanning for ship hull modelling, *Geosci.*, 9 (2019) 242. <https://doi.org/10.3390/geosciences9050242>
- [17] X. Jing, C. Zhang, Z. Sun, G. Zhao, and Y. Wang, The Technologies of Close-range Photogrammetry and Application in Manufacture, *Proc. 3rd Int. Conf. Mechatronics, Robot. Autom.*, 15 (2015) 988–994. <https://doi.org/10.2991/icmra-15.2015.192>
- [18] M. A. Thomas, M. F. Hassan, W. S. I. Wan Salim, S. A. Osman, H. Mustafa, and M. A. Jalal, Reconstruction of 3D models in automotive engineering applications using close-range photogrammetry approach, *J. Adv. Res. Fluid Mech. Therm. Sci.*, 61 (2019) 220–232.
- [19] A. Khalaf, T. Ataiwe, I. Mohammed, and A. Kareem, 3D Digital modeling for archeology using close range photogrammetry, *MATEC Web Conf.*, 162(2018) 162–165. <https://doi.org/10.1051/mateconf/201816203027>
- [20] F. M. Abed, M. U. Mohammed, M. U. Mohammed, and S. J. Kadhim, Architectural and Cultural Heritage conservation using low-cost cameras, *Appl. Res. J.*, 3 (2017) 376–384.
- [21] J. Sužiedelytė-Visockienė, R. Bagdžiūnaitė, N. Malys, and V. Maliene, Close-range photogrammetry enables documentation of environment-induced deformation of architectural heritage, *Environ. Eng. Manag. J.*, 14 (2015) 1371–1381, 2015. <https://doi.org/10.30638/eemj.2015.149>
- [22] M. A. Aguilar et al., Application of close-range photogrammetry and digital photography analysis for the estimation of leaf area index in a greenhouse tomato culture, *Int. Arch. Photogramm. Remote Sens. Spat. Inf. Sci. - ISPRS Arch.*, 38 (2010) 5–10.
- [23] D. J. Benton, A. J. Chambers, M. J. Raffaldi, S. A. Finley, and M. J. Powers, Close-range photogrammetry in underground mining ground control, *Remote Sens. Syst. Eng.*, 9977 (2016) 997707. <https://doi.org/10.1117/12.2236691>
- [24] D. A. Hussien, F. M. Abed, and A. A. Hasan, Stereo photogrammetry vs computed tomography for 3D medical measurements, *Karbala Int. J. Mod. Sci.*, 5 (2019) 201–212. <https://doi.org/10.33640/2405-609X.1130>
- [25] J. Yang, Q. Zhou, and Q. Wang, Close-range photogrammetry for the modelling of mouldboard plough surfaces, *PIAGENG 2013 Image Process. Photonics Agric. Eng.*, 8761 (2013) 87610D. <https://doi.org/10.1117/12.2019652>

- [26] A. Jameel, Establishment of 3D Model with Digital Non-Metric Camera in Close Range Photogrammetry, 31 (2013) 1601–1611.
- [27] A. Zedan Khalaf and A. J. Salah Al-Saedi, Assessment of Structure with Analytical Digital Close Range Photogrammetry, Eng. Technol. J., 34 (2016) 2140–2151. <http://dx.doi.org/10.30684/etj.34.11A.18>
- [28] T. N. Ataiwe, I. Hatem, and H. M. J. Al Sharaa, Digital Model in Close-Range Photogrammetry Using a Smartphone Camera, 04005 (2021) 1–11. <https://doi.org/10.1051/e3sconf/202131804005>
- [29] C. Vi and W. G. Vi, Digital Photogrammetry At Graduated Study in Uaceg, October, 2000.
- [30] S. M. Walker, A. L. R. Thomas, and G. K. Taylor, Photogrammetric reconstruction of high-resolution surface topographies and deformable wing kinematics of tethered locusts and free-flying hoverflies, J. R. Soc. Interface., 6 (2009) 351–366.
- [31] H. Rütger, J. Smit, and D. Kamamba, A Comparison of Close-Range Photogrammetry to Terrestrial Laser Scanning for Heritage Documentation, South African J. Geomatics., 1 (2012) 149–162–162.
- [32] B. Triggs, P. F. McLauchlan, R. I. Hartley, and A. W. Fitzgibbon, Bundle adjustment – a modern synthesis, Lect. Notes Comput. Sci. including Subser. Lect. Notes Artif. Intell. Lect. Notes Bioinformatics., 1883 (2000) 298–372, https://doi.org/doi:10.1007/3-540-44480-7_21
- [33] J. A. Doumit, From Drones to Geospatial Data, 2019.
- [34] N. Börlin, A. Murtiyoso, P. Grussenmeyer, F. Menna, and E. Nocerino, Flexible photogrammetric computations using modular bundle adjustment: The chain rule and the collinearity equations, Photogramm. Eng. Remote Sensing., 85 (2019) 361–368. <https://doi.org/doi:10.14358/PERS.85.5.361>
- [35] K. Jacobsen, Methods of Block adjustment and Analoge Adjustment, 1960.
- [36] K. L. A. El-Ashmawy, Block Adjustment Using Control Distances Constraint, Int. j. sci. res. Innov., 03 (2021) 253–257. <http://journalijisr.com/sites/default/files/issues-pdf/IJISRR-424.pdf>
- [37] N. Yastikli, I. Bagci, and C. Beser, The processing of image data collected by light UAV systems for GIS data capture and updating, Int. Arch. Photogramm. Remote Sens. Spat. Inf. Sci. - ISPRS Arch., 40 (2013) 267–270. <https://doi.org/doi:10.5194/isprsarchives-XL-7-W2-267-2013>
- [38] G. Vacca, “Overview of Open Source Software for Close Range Photogrammetry, Int. Arch. Photogramm. Remote Sens. Spat. Inf. Sci. - ISPRS Arch., 42 (2019) 239–245. <https://doi.org/doi:10.5194/isprs-archives-XLII-4-W14-239-2019>
- [39] W. Faig, Calibration of Close-Range Photogrammetric Systems: Mathematical Formulation., Photogramm. Eng. Remote Sensing., 41 (1975) 1479–1486.
- [40] D. T. Y. Al-Qaysi, Design A Criterion for the Determination of the Interior Orientation Parameters of Non-Metric (Digital Camera), M. Sc. Thesis submitted to the Universty of Technology- Iraq, 2016.
- [41] Instruction Manual Canon EOS 500D Digital Camera, Instruction Manual, Guide Book, South America, 2003.
- [42] D. George and P. Mallery, Simple Linear Regression, IBM SPSS Stat. 25 Step by Step, no. Ed 8, 207–221, 2020. <https://doi.org/doi:10.4324/9781351033909-22>
- [43] M. Otivation and I. Ntroduction, Machine Learning and Data Mining, 2012, <https://doi.org/doi:10.13140/RG.2.2.20395.49446/1>
- [44] B. B. Frey, Standard Error of Measurement, SAGE Encycl. Educ. Res. Meas. Eval., 2018, <https://doi.org/doi:10.4135/9781506326139.n658>
- [45] R. Gonzalez, Lecture Notes 7: Residual Analysis and Multiple Regression 7-1 Lecture Notes (7): Residual Analysis and Multiple Regression, Nonlinearity, 2 (2011) 1–22.
- [46] A. C. Cameron and F. A. G. Windmeijer, R-squared measures for count data regression models with applications to health-care utilization, J. Bus. Econ. Stat., 14 (1996) 209–220. <https://doi.org/doi:10.1080/07350015.1996.10524648>
- [47] N. Q. Long, X. Bui, N. V. Nghia, and P. Van Chung, Lightweight Unmanned Aerial Vehicle and Structure-from-Motion Photogrammetry for Generating Digital Surface Model for Open-Pit Coal Mine Area and Its Accuracy Assessment, Adv. Appl. Geospatial Technol. Earth Resour., 2017, 2018, <https://doi.org/doi:10.1007/978-3-319-68240-2>
- [48] D. K. Lee, J. In, and S. Lee, Standard deviation and standard error of the mean, Korean J. Anesthesiol., 68 (2015) 220–223. <https://doi.org/doi:10.4097/kjae.2015.68.3.220>